Scientific Reports

https://doi.org/10.1038/s41598-025-32516-7

Article in Press

An aptamer-functionalized AuNPs/rGO nanocomposite biosensor for ultrasensitive detection of foodborne pathogen *E. coli O157:H7*

Received: 1 August 2025

Accepted: 10 December 2025

Published online: 08 January 2026

Cite this article as: Izadi M. & Arvand M. An aptamer-functionalized AuNPs/rGO nanocomposite biosensor for ultrasensitive detection of foodborne pathogen *E. coli O157:H7*. *Sci Rep* (2026). https://doi.org/10.1038/s41598-025-32516-7

Mohadeseh Izadi & Majid Arvand

An aptamer-functionalized AuNPs/rGO nanocomposite biosensor for ultrasensitive detection of foodborne pathogen *E. coli O157:H7*

Mohadeseh Izadi, Majid Arvand*

Electroanalytical Chemistry Laboratory, Faculty of Chemistry, University of Guilan, Namjoo Street, P.O. Box: 1914–41335, Rasht, Iran

*Corresponding author. Tel.: +98 13 33233262, fax: +98 13 33233262

E-mail address: arvand@guilan.ac.ir (M. Arvand)

ORCID iD: 0000-0002-5824-8688

Abstract

Foodborne pathogenic bacteria can cause food poisoning or infection, leading to disease. Early screening of foodborne pathogens has become crucial for managing and preventing these diseases. Here, we developed an electrochemical aptamer-based biosensor to detect *Escherichia coli* (*E. coli O157:H7*) in real samples. The glassy carbon electrode (GCE) underwent an initial treatment using a nanocomposite made of reduced graphene oxide (rGO) and gold nanoparticles (AuNPs) (AuNPs/rGO/GCE) to enhance the surface area and boost the sensor's sensitivity. In addition to good electrical properties, nanocomposites made of rGO and AuNPs play a crucial role in sensor development by enabling high loading and adequate immobilization of biorecognition elements like aptamers while preserving their activity and affinity. Next, to elevate the specificity of the altered electrode, aptamers were linked to the exterior of the prepared electrode (APT/AuNPs/rGO/GCE). The prepared electrode underwent characterization using field emission scanning electron microscopy, energy-dispersive spectroscopy, Fourier-transform infrared spectroscopy, and electrochemical impedance spectroscopy. This proposed aptasensor can accurately identify *E. coli O157:H7* within a range of 6 to 6 × 10^8 CFU/mL and has a detection limit of 3.25 CFU/mL. Microbial culture results validate the aptasensor findings, providing quicker results and a lower detection limit.

Keywords Aptasensor, Electrochemical biosensor, *Escherichia coli*, Nanomaterial

Introduction

Food and waterborne illnesses caused by pathogenic *Escherichia coli* (*E. coli*) strains are a significant factor in the high sickness rates in numerous developing nations[1]. These enteric bacteria cause infections by penetrating the intestinal lining in humans, resulting in gastroenteritis and other related illnesses that can be life-threatening[2]. *E. coli O157:H7* is one of the essential strains of *E. coli* that cause severe intestinal infections in humans. This strain is the most common cause of human infection and is recognized as a significant foodborne pathogen. Symptoms of infection caused by *E. coli O157:H7* include severe diarrhea (often bloody) and abdominal pain[3]. *E. coli O157:H7* is the leading cause of hemorrhagic colitis and, critically, Hemolytic Uremic Syndrome (HUS), a life-threatening complication involving acute kidney failure, which elevates this organism far above most other *E. coli* infections in terms of public health urgency. Furthermore, unlike ETEC, *E. coli O157:H7* has an extremely low infectious dose estimated to be fewer than 100 cells[4]. Therefore, creating a point-of-care biosensor device is necessary

to quickly and precisely detect *E. coli O157:H7*[5]. Various methods have been utilized to identify harmful bacteria, such as traditional culturing methods, enzyme-linked immunosorbent assay (ELISA), and polymerase chain reaction (PCR). Traditional cultural techniques are dependable but require significant work and time (at least 1-2 days)[6]. ELISA typically takes at least 24 to 28 hours to complete, and its sensitivity is insufficient to detect low levels of pathogens[7]. The PCR method offers unique sensitivity benefits but frequently faces issues with false positive results and a complicated pretreatment process[8]. Compared to these techniques, biosensors provide a different, easier, and more cost-effective approach to detecting pathogens[9]. Electrochemical biosensors detect an analyte based on the change in response due to the electrochemical interaction between the analyte and the electrode surface[10].

Advancements in nanomaterials and signal amplification strategies have significantly enhanced the detectability of electrochemical sensing techniques. Due to their distinct characteristics, various nanomaterials, such as gold nanoparticles (AuNPs) and compounds with a carbon source like graphene, have been utilized as electrode materials to develop sensing platforms[11].

Graphene, a material that is only one atom thick and two-dimensional, has been the focus of much interest due to its high electron mobility and low electrical resistivity. However, graphene must be functionalized with chemical groups before additional utilization to enhance its usability due to

its hydrophobic nature[12]. Graphene oxide (GO) serves as the supporting structure for electrochemically deposited nanoparticles during biomolecule immobilization, but the oxygen groups in GO diminish the effectiveness of heterogeneous electron transfer. In contrast, reduced graphene oxide (rGO) offers excellent electrical conductivity and a high specific surface area due to the presence of various organic functional groups such as –OH and –COOH. The carboxyl groups have a greater tendency to interact with biomolecules (enzymes, proteins, nucleic acids) on the rGO surface[13]. The inert chemical properties, high current density, and extreme hydrophobicity at the nanoscale of rGO enable its use as a conductive foundation in creating electrochemical biosensors[14].

Noble metal nanoparticles (MNPs), such as silver and gold, display distinct chemical and physical traits, including electronic, optical, magnetic, and catalytic attributes, compared to their larger forms[15]. Due to their smaller size, AuNPs exhibit high absorption capacity, excellent stability, and strong conductivity. AuNPs have also been widely employed in creating electrochemical sensors[16].

The combination of graphene's high electron mobility and AuNPs has attracted considerable interest in electrocatalysis, and the potential to reduce sheet resistance in rGO-based devices has generated significant interest in electronic and electrochemical applications. Incorporating AuNPs into graphene nanosheets can effectively improve sensor sensitivity and detection limit by enhancing electron transfer or catalyzing reactions with

specific analytes[17]. Composites of rGO and AuNPs show improved performance due to their synergistic effects compared to using only rGO or AuNPs separately. The merging of rGO and AuNPs prevents them from undergoing restacking and offers a new method for creating high-tech composite materials suitable for various applications[18]. AuNPs further enhance the characteristics of rGO by creating an appropriate microenvironment for biosensors, enabling easy surface modification. Currently, there are multiple methods for creating AuNPs-decorated graphene nanocomposites[19]. The electrochemical deposition technique generally results in stable nanoparticles with small size and large surface area[16]. The electrodeposition method is frequently used to deposit alloys and high-grade semiconductors. By using this method, factors such as the size, density, and composition of alloys, as well as the morphology of nanoparticles, can be accurately controlled by adjusting the electrodeposition potential, charge, duration, concentration, and composition of the metal precursor solutions[20].

On the other hand, aptamers, antibodies, and enzymes have been used more frequently as recognition biomolecules in biosensors[21]. Aptamers are synthetic DNA or RNA strands that are obtained from random sequence nucleic acid libraries through a process called Systematic Evolution of Ligands by Exponential Enrichment (SELEX)[22] and can precisely identify specific target molecules like proteins, drugs, toxins, amino acids, vitamins, and even entire cells. Aptamers, acting as a clever solution, demonstrate

precision and intense attraction to their specific targets (similar to the lock-and-key relationship of antibodies and antigens), making them suitable as biological recognition elements for electrochemical tests[23]. Aptasensors are biosensors that use aptamers as the recognition biomolecule[24]. Various aptasensors have been created by scientists using different sensing platforms[25]. In 2012, Queirós and colleagues developed a DNA aptamer-based impedance biosensor without labels to detect outer membrane proteins of *E. coli*. Two single-stranded DNA sequences were evaluated as recognition components. The aptamer binding probes were attached to a gold electrode, both with and without 6-mercapto-1-hexanol. Faradaic impedance spectroscopy was utilized to characterize each stage of the modification process[26]. In 2017, Brosel-Oliu and his team created an impedimetric transducer modified with an *E. coli*-specific aptamer. It featured a three-dimensional interdigitated electrode array, with electrodes separated by insulating barriers. A DNA aptamer was chosen as the biorecognition element for its ability to precisely identify the outer membrane proteins of *E. coli O157:H7*[27]. In 2021, Qaanei and colleagues developed an electrochemical aptasensor to detect *E. coli O157:H7* by utilizing a nanocomposite containing reduced graphene oxide, gold nanoparticles, and polyvinyl alcohol. Probe DNA of *E. coli O157:H7* was prepared using a solution of rGO and PVA, which was then applied to the surface of the glassy carbon electrode (GCE). In the next step, AuNPs/rGO-PVA/GCE was prepared by depositing the AuNPs

dispersion onto the rGO-PVA/GCE surface. Next, a drop of the thiolated aptamer solution was placed onto the AuNPs/rGO-PVA/GCE[28].

In this study, we designed a specific electrochemical aptasensor using an amino aptamer-immobilized AuNPs/rGO composite as a conductive platform for detecting foodborne pathogens. The APT/AuNPs/rGO aptasensor was prepared using an rGO and AuNPs composite decorated onto a GCE for *E. coli O157:H7*, which is a cheap, sensitive, and practical method for detecting low concentrations of bacteria in a short period. Additionally, the possible use of the proposed biosensor in actual food systems was explored effectively.

Materials and methods

Reagents and apparatus

Potassium nitrate, potassium chloride, methanol, Nafion, dimethylformamide (DMF), potassium hexacyanoferrate ($K_3[Fe(CN)_6]$), 1-ethyl-3-(3-dimethylaminopropyl) carbodiimide hydrochloride (EDC), N-hydroxysuccinimide (NHS), bovine serum albumin (BSA), hydrogen tetrachloroaurate(III) ($HAuCl_4$) were procured from Merck, Darmstadt, Germany. Reduced graphene oxide (rGO) bought from US Nano Company. An ssDNA APT for *E. coli O157:H7* was employed as the targeting ligand. The sequence of the NH_2-functionalized APT was:

5′-NH_2-(-CCGGACGCTTATGCCTTGCCATCTACAGAGCAGGTGTGACGG-)3[29,30]

With the complete sequence synthesized by Optical Density, OD = 4, T_m= 79.4 °C, and Purification: HPLC from Bioneer® Corporation. The aptamer solution was stored at -20 °C. *Escherichia coli* and all other bacteria used in this study, including *Salmonella typhimurium*, *Pseudomonas aeruginosa,* and *Staphylococcus aureus, E. coli* K-12, were obtained from the Iranian Research Organization for Science and Technology (IROST). Eosin methylene blue (EMB) and MacConkey agar medium were purchased from Merck, Darmstadt, Germany. Electrochemical experiments, such as differential pulse voltammetry (DPV), cyclic voltammetry (CV), and electrochemical impedance spectroscopy (EIS), were conducted in a mixed solution containing 0.1 M KCl and 5 mM hexacyanoferrate on a potentiostat/galvanostat Autolab PGSTAT 30 produced in the Netherlands. The classical three-electrode setup, which includes a glassy carbon electrode (diameter = 2 mm), a platinum electrode, and an Ag/AgCl electrode (saturated KCl) defined as working, auxiliary, and reference electrodes, was utilized for electrochemical assessments. Morphological analysis of the modifiers was successfully performed using a field emission scanning electron microscope (FESEM, Mira3 XMU from TESCAN Company) coupled with energy dispersive X-ray spectroscopy (EDS). Fourier transform infrared (FT-IR) spectra were obtained in KBr pellets across the 4000−400 cm^{-1} frequency range utilizing a Tensor 27 from Bruker. Bacteria stock solution concentration was determined using the Perkin Elmer spectrophotometer.

Fabrication of AuNPs/rGO

Various techniques have been documented for synthesizing diverse metal nanoparticles (MNPs)/rGO nanocomposites, including microwave irradiation[31], chemical reduction[32], electrochemical deposition[33], photochemical reduction[15], sonochemical reduction[34], and thermal reduction[35]. Electrochemical deposition efficiently produces high-purity MNPs on rGO sheets, making it a straightforward and rapid method. This technique creates metal nanoparticles on GCEs coated with rGO. The process involves three main steps: (1) arranging rGO sheets onto an electrode, (2) immersing the graphene-coated electrode in an electrolytic solution containing metal precursors, and (3) applying an appropriate voltage.

To prepare the working electrode, the first step involved polishing a bare GCE using 0.3 μm and 0.05 μm alumina powder. This polishing process is crucial for ensuring a smooth and clean electrode surface, which is necessary for optimal electrochemical performance. After polishing, the electrode was sonicated in a 1:1 solution of deionized water and ethanol for 5 minutes. This step is vital as it helps remove any physically adsorbed substances that may remain on the electrode surface after polishing. Once the electrode was thoroughly cleaned, the next step was to apply a thin layer of rGO to the surface. To achieve this, five microliters of rGO solution, which had a concentration of 2000 μg/mL and included 0.1% Nafion, was placed on the surface of the GCE. This application was performed in two steps to ensure an

even distribution and sufficient coating of the rGO on the electrode surface. The presence of Nafion aids in stabilizing the rGO dispersions and enhances the adhesion of the rGO layer, thereby facilitating improved electrochemical interactions during subsequent experiments[36]. The electrodeposition process on the working electrode was conducted using CV in a $HAuCl_4$ solution with a concentration of 0.1%. During the electrodeposition, 10 cycles were applied within a potential range spanning from -1.4 to +0.6 V. The scan rate was controlled at 0.1 V/s to achieve optimal deposition conditions and ensure precise measurement of the current response throughout the process. Distilled water was used to rinse the electrode between steps, ensuring removal of any loosely adhered substance.

Fabrication of electrochemical aptasensor

The organic functional groups on the surface of the AuNPs/rGO were coupled to the NH_2-functionalized *E. coli*-specific aptamer using EDC/NHS chemistry. The modified electrode should be incubated in a solution (0.5 mg/mL) of EDC/NHS for 2 hours after depositing a thin layer of AuNPs/rGO on the working electrode. Subsequently, 5 µL of amino-modified APT (7 µM) was placed onto the electrode. The electrostatic interaction between the amine and carboxyl groups immobilizes the APT on the electrode surface. The final aptasensor was stored at 4 °C when not in use. This aptasensor should be treated with a bovine serum albumin (1%, 60 min) solution before pairing with *E. coli O157:H7* to prevent nonspecific binding and obstructing the

unoccupied sites. The aptasensor APT/AuNPs/rGO/GCE, which serves as a probe for *E. coli O157:H7* capture, was incubated with different concentrations of *E. coli O157:H7* solution, and DPV was used to study it. The DPV method was used with a modulation amplitude of 25 mV, a step potential of 5 mV, a modulation time of 0.05 s, and an interval time of 0.5 s. The CV method was utilized with a potential scan from -0.4 to +0.8 V at a scan rate of 0.1 V/s. The EIS measurements were performed over a frequency range from 5 mHz to 100 kHz using a sinusoidal signal of 10 mV and at a DC potential of 0.25 V versus Ag/AgCl. The modified electrode's performance was evaluated through the electrochemical methods mentioned previously in a three-electrode cell assembly with a redox probe containing 5 mM $K_3[Fe(CN)_6]$, which included 0.1 M KCl.

Bacteria preparation and detection

The *E. coli O157:H7* bacteria strain (PTCC 1860) was obtained from the IROST. It was first grown in a sterilized EMB agar medium at 37 °C for 16 hours[37]. Next, the plate counting method was used to determine the purity of the suspension. At 600 nm, OD was used to determine the concentration of the stock solution. The correlation between standard plate count and OD measurements was determined by comparing them. As a stock, the most recent solution was utilized. The bacterial stock culture was diluted in phosphate buffer solution (PBS, 0.1 M, pH = 7.4) to achieve more dilute concentrations. The confirmation of the strain’s identity is robust, relying on

both certified procurement standards and the inherent specificity of our molecular recognition element. The *E. coli O157:H7* strain used throughout this study, PTCC 1860, was obtained directly from a certified biological resource center (Persian Type Culture Collection), which guarantees its initial characterization and purity, serving as the foundational confirmation of its identity. For routine laboratory maintenance and initial quality checks, the strain's identity was further verified using selective media. Specifically, the utilization of Eosin Methylene Blue (EMB) agar confirmed the sugar-fermenting nature of the *E. coli* by producing the characteristic metallic green sheen. Additionally, Sorbitol MacConkey Agar (SMAC) supplemented was employed. This relied on the known metabolic feature of *E. coli O157:H7* (its inability to ferment sorbitol) which results in colorless colonies compared to most other *E. coli* strains.

Electrochemical detection of *E. coli O157:H7*

To detect bacteria, the aptasensor was immersed in a bacterial solution within a PBS (0.1 M, pH = 7.4) for 60 minutes (optimized time for target binding). The electrode was thoroughly washed with PBS (pH 7.4) to remove unbound bacteria. Afterward, it was submerged in 50 mL of the mixture containing 5.0 mM K_3 [Fe $(CN)_6$]) and 0.1 M KCl, and the differential pulse voltammogram was recorded. Different concentrations of *E. coli O157:H7* from 6 to 6 × 10^8 CFU/mL were tested using the aptasensor. The data was used to create a calibration plot, and the detection limit was subsequently

determined. The prepared samples were deliberately spiked with *E. coli O157:H7* to achieve specific final concentrations of 6 × 10^4 and 6 × 10^6 CFU/mL. For every sample, DPV was conducted, and based on the calibration graph, the recovery rate and relative standard deviation (RSD) were calculated. Water collected from poultry farms was selected as the sample for this study. Poultry farm water samples confirmed to be free of bacteria by culture plating were used as the actual matrix for spiking with pure cultures of pathogenic *E. coli O157:H7* at defined concentrations. For each analyzed sample, the results from DPV were compared to those obtained from the plate counting method. The significance of the differences between the two methods was evaluated using *p*-values.

Antibacterial test

The effects of various antibacterial agents were thoroughly evaluated, with a specific focus on enrofloxacin, a fluoroquinolone antibiotic recognized for its strong efficacy against *E. coli O157:H7* and Water Guard, an acidifier that inhibits intestinal pathogens by disrupting bacterial cell membranes. In this study, 10 µL of enrofloxacin (10%) was added to 10 mL of a solution containing *E. coli O157:H7*. In a separate experiment, 10 µL of the acidifier was used under the same conditions. The aptasensor can capture electrochemical signals using the DPV technique after incubating *E. coli O157:H7* with these antibacterial agents for four hours. The single-dose evaluation method was used in this experiment.

Results and discussion

Design of electrochemical aptasensor for *E. coli O157:H7* detection

The diagram illustrating the construction process of the electrochemical aptasensor is shown in Scheme 1. First, a layer of rGO was cast on a GCE, followed by the electrodeposition of AuNPs on the working electrode. Electrons can quickly transfer from the GCE to AuNPs/rGO. The biosensor contained an amino-aptamer immobilized on an AuNPs/rGO composite as a conductive platform on the GCE surface via carboxylic amine binding. The organic functional groups on the surface of the AuNPs/rGO were coupled to the NH_2-functionalized *E. coli*-specific aptamer using EDC/NHS chemistry. EDC was used to covalently bond the carboxylic groups on the AuNPs/rGO interface, releasing 1-ethyl-3-(3-dimethylaminopropyl) urea when it reacted with NHS to activate the carboxyl groups. This connection promotes the development of a strong bond, guaranteeing that the aptamer stays securely attached to the electrode. It enhances the binding of APT and maintains its structural integrity on the surface during subsequent reactions or measurements. Signal detection and electrochemical measurements were accomplished using a K_3 [Fe $(CN)_6$] redox probe when *E. coli O157:H7* was present. This aptasensor underwent incubation in a bovine serum albumin solution to block off the unspecific area before pairing with *E. coli O157:H7*.

“Please insert Scheme 1 here”

Morphological characterization

Fig. 1A displays several FESEM images depicting the surface structures of the modified electrodes on a fluorine-doped tin oxide-coated glass slide (FTO glass) at three magnifications. Fig. 1A(a, a', and a'') shows the surface structure of the modified electrode containing rGO. The rGO layer on the surface of the electrode can increase its surface area. The FESEM image of the rGO film demonstrated a consistent distribution of rGO plates. Fig. 1A(b, b', and b'') shows the surface structure of the modified electrode containing AuNPs/rGO, demonstrating the electrodeposition of gold nanoparticles on rGO. The size of the particles in the image with 75 kX magnification is about 81 nm. The nanostructure showed that it is a contributory factor for increasing the surface area, as well as providing more linkage sites for APT loading. The FESEM image of the APT/AuNPs/rGO film showed that the size of the particles in the image with 75 kX magnification is about 298 nm (Fig. 1A(c, c', and c'')). This increase in size is mainly due to the aptamer molecules binding to the surface of the AuNPs and rGO, forming a coating layer that increases the overall particle size. Additionally, aptamer binding can induce some aggregation or cluster formation, which further contributes to the larger observed size. This expected size expansion confirms the successful functionalization and successful binding of the aptamer molecules, validating the performance of the final APT/AuNPs/rGO structure. Moreover, the EDS spectrum in Fig. 1B(a-c) demonstrates rGO, AuNPs/rGO, and APT/AuNPs/rGO film, respectively. The EDS spectrum of rGO shows signals for carbon and

oxygen, with weight percentages of 71.8% and 25.4%, respectively (Fig. 1B(a)). The EDS spectrum of the AuNPs/rGO nanocomposite film on FTO in Fig. 1B(b) shows signals for carbon, oxygen, and Au with weight percentages of 56.5, 11.07, and 27.27%, respectively. Fig. 1B(c) shows the EDS spectrum of the APT/AuNPs/rGO film on FTO. The EDS spectrum of APT/AuNPs/rGO shows signals for carbon, oxygen, Au, and N with weight percentages of 58.3, 18, 15.28, and 4.37%, respectively (Signals related to FTO were omitted).

FT-IR spectroscopy was used to study the interactions among the rGO sheets, AuNPs, and APT. Fig. 1C gives the FT-IR spectra of rGO, AuNPs/rGO, and APT/AuNPs/rGO. The spectrum of rGO shows a broad absorption band at 3428 cm^{-1} corresponding to the stretching vibration of O−H, and peaks in wave numbers of 2921 and 2824 cm^{-1} correspond to the asymmetric and symmetric CH_2 stretching of rGO. The IR peaks at 1056 cm^{-1} and 1220 cm^{-1} are attributed to the stretching of the carbon-oxygen (C−O) bond. In addition, an absorption peak observed at 1712 cm^{-1} is attributed to the presence of carbonyl (C=O) functional groups. These functional groups play a significant role in biochemical interactions, as they are capable of reacting with various other functional biomaterials, notably including aptamer chains. The magnitude of C=C band at 1631 cm^{-1} increased in the AuNPs/rGO spectrum. After aptamer bonding on the surface of AuNPs/rGO, absorption peaks related to C−N groups at 1113 cm^{-1} presented in the APT/AuNPs/rGO spectrum.

“Please insert Fig. 1 here”

Electrochemical characterization of electrochemical aptasensor

Electrochemical techniques were used to study the modification process of the electrode. $[Fe(CN)_6]^{3-/4-}$ (5 mM) was selected as the electroactive probe for studying the voltammogram changes. Fig. 2A displays the cyclic voltammograms of various modification stages: the bare GCE (curve a), rGO/GCE (curve b), AuNPs/rGO/GCE (curve c), APT/AuNPs/rGO/GCE (curve d), and *E. coli*/APT/AuNPs/rGO/GCE (curve e) at a scan rate of 100 mV/s. This figure demonstrates that the peak current (I_p) of rGO/GCE (curve b) is higher than the peak current of the bare electrode (curve a). The increased peak current intensity could be attributed to the larger surface area and higher conductivity of the modification layer on the electrode's surface. Following the electrodeposition of AuNPs on the modified electrode, a notable rise in the current peak was detected, suggesting enhanced electrical conductivity and an increase in the electrode's surface area. Electron transfer becomes easier due to the topological electrical contact points through the matrix (curve c). The electrostatic interaction between APT's amino group and the carboxylate group of the nanocomposite on the electrode surface caused electron transfer to be difficult due to the nucleic acid structure. Some active sites were blocked, resulting in reduced peak current (curve d). Finally, when an *E. coli O157:H7* interaction with APT was taken, the process for electron transport was more complicated than the previous step and observed more reduction in peak current, which shows *E. coli O157:H7* was attached

successfully to the electrode surface and blocked the electron transfer (curve e). Following CV assessment in the probe solution, the electrode's electrochemical performance was evaluated using DPV, yielding similar results (Fig. 2B). When the bare electrode was modified with rGO, an increase in peak current was observed. This was due to the larger surface area and higher conductivity of the modification layer on the electrode's surface (curve b). After electrodepositing AuNPs onto the modified electrode, a significant rise in peak current was noted for the reasons explained in the CV section (curve c). When APT was applied to the surface of the modified electrode, there was a decrease in peak current because active sites were blocked (curve d). When the aptasensor was incubated in an *E. coli O157:H7* solution (6×10^5 CFU/mL), the binding between *E. coli O157:H7* and APT led to a decrease in electron transfer and conductivity on the modified electrode surface, which ultimately resulted in a reduction of peak current (curve e). Next, the electrochemical performance of the electrode was evaluated with EIS measurements in the probe solution, yielding comparable results. The Nyquist plots associated with various modified electrodes are displayed in Fig. 2C. When the bare electrode (R_{ct} =117 Ω, curve a) was modified by rGO, a decrease was seen in R_{ct} (R_{ct} =113 Ω, curve b). As mentioned, it was due to the structure of the rGO. After the electrodeposition of AuNPs on the modified electrode, R_{ct} dropped again (R_{ct} =102 Ω, curve c). It indicates a decrease in resistance due to an increase in the speed of electron transfer. When APT was placed on the surface of the modified electrode, there was a pronounced

increase in R_{ct} (R_{ct} =153 Ω, curve d). Finally, the most R_{ct} (R_{ct} =196 Ω, curve e) was observed from the aptasensor incubated in an *E. coli O157:H7* solution (6×10^5 CFU/mL). By binding *E. coli O157:H7* with APT, electron transfer on the modified electrode surface and its conductivity decreased. Fig. 2D show the DPV comparing the bare GCE (curve a), modified with AuNPs (curve b), and with rGO (curve c) against the full AuNPs/rGO composite (curve d). When rGO is deposited alone onto a GCE, its layered, highly porous structure provides a very large electroactive surface area. This increases the effective contact with the electrolyte, enhancing the double-layer capacitance and charge-transfer rate. Consequently, both the baseline current and DPV peak currents rise noticeably. In contrast, when AuNPs are deposited alone without a conductive porous substrate, they tend to form small isolated islands or dense agglomerates. surface blocking lowers the double-layer capacitance, leading to a decrease in baseline current compared to bare GCE. When the rGO/AuNPs composite is deposited, the large surface area and continuous conductive pathways of rGO provide an excellent scaffold for the uniform dispersion of AuNPs. The gold nanoparticles, in turn, act as highly efficient catalytic sites for charge transfer, while rGO maintains a high electroactive area. This synergy between rGO's high electrical conductivity and AuNP's strong electrocatalytic properties dramatically reduces the charge-transfer resistance (R_{ct}) and results in a pronounced increase in baseline and DPV peak currents.

"Please insert Fig. 2 here"

Optimization of the experimental conditions

To achieve the highest sensitivity in measuring *E. coli O157:H7* bacteria, various parameters were optimized. The optimization was done using the method of one factor at a time. In other words, in each step of the optimization process, only one factor was changed to be optimized, and all other factors were considered constant on the electrochemical response of the aptasensor. Finally, the optimal conditions were used to continue the experiments.

The effect of rGO concentration on the peak current

The impact of rGO concentration on the peak current was examined. As shown in Fig. 3A, the current value increases significantly when the rGO concentration rises from 1000 to 2000 µg/mL. This suggests that there is a greater active surface area and an acceleration of electron transfer as the amount of rGO increases. Afterward, the growth slows down significantly at concentrations higher than 2000 µg/mL. Exceeding the optimal point promotes severe π to π stacking and aggregation of the rGO sheets, which destroys the critical porous network and significantly increases the Ohmic resistance by lengthening the electron transport distance from the solution-based redox probe to the underlying electrode. Consequently, mass transfer becomes the limiting factor for the current, as the thick, aggregated film restricts the diffusion of the redox ions to the surface. The current does not

change much due to the increase in surface thickness. In the following experiments, the optimal concentration of rGO is 2000 µg/mL.

The effect of Au concentration on the peak current

The concentration of electrochemically deposited $HAuCl_4$ salt on the surface of the rGO/GCE electrode was investigated. As shown in Fig. 3B, the intensity of the peak current gradually increased with increasing $HAuCl_4$ salt concentration. The changes in current intensity reached their maximum when the $HAuCl_4$ salt concentration was 0.1%. When the concentration of $HAuCl_4$ exceeded 0.1%, the peak current value began to decrease. Using this behavior, it is apparent that an excess $HAuCl_4$ concentration can hamper electron transfer due to the increase in the density of gold nanoparticles and the decrease in electron transfer kinetics. To optimize the concentration of Au in the upcoming experiments, a concentration of 0.1% was used.

The effect of APT concentration on the peak current

To optimize the quantity of aptamer immobilized on the surface of the modified electrode, concentrations of 2, 5, 7, 10, and 15 µM of aptamer were investigated. As shown in Fig. 3C, the ΔI_p value ($\Delta I_p = I_{p(modified)} - I_{p(aptamer)}$) gradually increased with aptamer concentration. The changes in current intensity reached their maximum when the aptamer concentration was 7 µM. After that, when the aptamer concentration exceeded 7 µM, the ΔI value decreased. This behavior shows that excessive aptamer concentration can

hinder electron transfer due to increased steric hindrance. A concentration of 7 μM was chosen as the optimal concentration in the following experiments.

The effect of aptamer incubation time

By increasing the incubation time of the aptamer on the modified electrode surface from 1 to 12 hours, an increase in the ΔI_p was observed (Fig. 3D), which indicates the time required to bind the amine group of the aptamer to the carboxyl group of the nanocomposite in the presence of the NHS/EDC. After more than 12 hours and up to 24 hours, a decrease in the ΔI_p was observed, indicating that the reaction is complete after 12 hours. The optimal aptamer incubation time for the following experiments was 12 hours.

The effect of *E. coli O157:H7* incubation time

As shown in Fig. 3E, an increase in the ΔI_p ($\Delta I_p = I_{p(aptamer)} - I_{p(aptamer/E.\ coli\ O157:H7)}$) was observed by increasing the incubation time of the modified electrode in bacteria (6×10^4 CFU/mL) from 10 to 120 minutes, which indicates the time required for the complete binding of the bacteria to its specific aptamer. Still, after more than 60 to 120 minutes, a small increase in the ΔI_p was observed, which indicates that the formation of the aptamer-*E. coli O157:H7* complex has reached saturation. Therefore, 60 minutes was the optimal time for *E. coli O157:H7* incubation in the following experiments.

“Please insert Fig. 3 here”

Calibration curve of biosensor

Fig. 4 shows the differential pulse voltammograms of the aptasensor in response to different concentrations of *E. coli O157:H7*. The data show a progressive decline in the DPV peaks as the concentration of *E. coli O157:H7* increases, ranging from 6 to 6 × 10^8 CFU/mL. This decrease is attributed to the increasing difficulty of electron transfer as the concentration of bacteria rises. The formation of a bacterial complex and its specific aptamer on the electrode's surface hinders the electron transfer process of the redox pair, leading to a reduced peak current in the differential pulse voltammogram. A compelling linear relationship with a good R^2 value demonstrates the correlation between ΔI_p and bacterial concentration. By analyzing the data, a linear equation was obtained: $\Delta I_p = 0.4\log C + 3.93$, in which $\Delta I_p = I_{p(aptamer)} - I_{p(aptamer/E.\ coli\ O157:H7)}$, and C is the concentration of *E. coli*. The limit of detection (LOD) of the proposed method was calculated to be 3.25 CFU/mL based on three times the standard deviation of the blank sample/slope. The LOD for the proposed method was calculated using the standard deviation of the blank samples, which is a statistically rigorous approach. The LOD was determined based on the following criterion:

LOD = 3 × standard deviation of the blank sample/slope of the calibration curve (1)

The obtained LOD and linear range values were compared with those of other methods and are listed in Table 1.

"Please insert Fig. 4 here"

"Please insert Table 1 here"

Determination of *E. coli O157:H7* in real samples

To evaluate the effectiveness of the developed method, the constructed aptasensor was employed for recovery tests in various concentrations. The prepared samples were intentionally spiked with *E. coli O157:H7* to assess recovery rates and variability. These samples were fortified with precise concentrations of *E. coli O157:H7*, precisely at 6×10^4 and 6×10^6 CFU/mL of *E. coli O157:H7*. This fortification method ensured that the presence of the bacteria could be accurately evaluated. The recoveries for the various samples were meticulously measured, 98.1% and 95.3%, indicating that the methodology yielded highly effective results in detecting and quantifying *E. coli O157:H7* in the samples. Additionally, the RSD was calculated to be between 4.23% and 2.64%, reflecting a commendable level of precision and consistency in the measurements across the samples tested. The results in Table 2 confirmed the acceptable potential and feasibility of the fabricated aptasensor for the simple, accurate, and fast determination of *E. coli O157:H7* in spiked samples.

"Please insert Table 2 here"

The applicability of the proposed strategy was evaluated through the detection of *E. coli O157:H7* in water collected from poultry farms. This process involves collecting samples from different water sources from poultry farms and analyzing them to identify the presence of *E. coli O157:H7* bacteria. To ensure the accuracy and reliability of the results, the findings from the detection method were further validated using the plate counting method, which involves culturing the bacteria on agar plates to quantify their concentration. This comprehensive approach allows for a thorough assessment of the strategy's effectiveness in identifying *E. coli O157:H7* contamination in water samples. In the electrochemical detection method, water samples are incubated with the biosensor. Concurrently, parallel *E. coli O157:H7* samples from the same water samples are measured using the plate counting method. The results of the DPV test were compared to the plate counting method in Table 3. The results obtained from these two methods are consistent in magnitude, although the specific values show slight differences. The *p*-values calculated are significantly above 0.05, indicating no significant difference between our method and the plate counting method in these two groups. The detection time for the plate counting method is 48 hours, while our proposed method only takes about one hour. This substantial reduction in detection time will significantly enhance efficiency and broaden the potential applications of the method in the future.

“Please insert Table 3 here”

Stability and reproducibility

To assess the stability of the aptasensor, an electrode was prepared and stored at 4 °C before being used to detect *E. coli*. Two weeks later, its detection response for *E. coli O157:H7* remained at 96.01% of the original response. To assess the reproducibility of the aptasensor, it was constructed five separate times following an identical fabrication method. Each of these instances was tested for its ability to detect a concentration of 6×10^5 CFU/mL. After the measurements, the RSD was calculated to be 2.28%. This relatively low RSD value suggests that the aptasensor exhibits satisfactory reproducibility, indicating consistency in its performance across multiple trials. Reproducibility assessment between different batches of electrodes was conducted using three independent batches, each consisting of four electrodes. Following data collection, statistical analysis was performed using one-way ANOVA, which revealed no significant differences between batches ($p = 0.083$). The findings confirm the satisfactory reproducibility of the aptasensor, supporting its reliability for practical applications.

Specificity of the electrochemical aptasensor

To evaluate how well our aptasensor can identify specific bacteria while ignoring others, we carried out a set of experiments. We tested the sensor against four types of bacteria that are not our primary target: (a) *Salmonella typhimurium*, (b) *Pseudomonas aeruginosa*, and (c) *Staphylococcus aureus*, which can cause various infections and non-pathogenic strain *E. coli* K-12. By

including these common bacteria in our tests, we aimed to see how effectively our aptasensor can focus on the target bacteria while ignoring these non-target strains. We selected these organisms because they are commonly found in both clinical and environmental settings, which enable us to effectively assess the performance of the aptasensor against prevalent microbial threats. All bacterial species were tested under standardized experimental conditions, maintaining a constant concentration of 6×10^5 CFU/mL for each species. The response of the aptasensor was measured to assess its specificity. As shown in Fig. 5, the peak current difference ($\Delta I_p = I_{p(aptamer)} - I_{p(aptamer/bacteria)}$) recorded in the presence of non-target bacteria was minimal. The peak current values for the non-target bacteria were similar to the aptasensor current when *E. coli O157:H7* was absent (inset of Fig. 5). The findings indicate that the performance of the aptasensor was largely unaffected by the presence of other bacterial species. This shows that the aptasensor is highly selective for *E. coli O157:H7*, effectively distinguishing this target bacterium from others in the tested group. Overall, the results confirm the aptasensor's potential as a reliable tool for detecting *E. coli O157:H7* in various samples while minimizing interference from non-target organisms.

“Please insert Fig. 5 here”

Antibacterial test

A thorough and systematic investigation was conducted to examine the effects of different antibacterial agents on the pathogenic strain of *E. coli O157:H7*. These antibacterial agents work by adhering to the bacterial cell walls and penetrating the membrane, which disrupts the bacteria's structure and functions. This research specifically examined the impact of enrofloxacin, a fluoroquinolone antibiotic known for its effectiveness in treating infections in pets and domestic animals[38]. The evaluation was conducted using a specially designed aptasensor, an innovative tool that enables precise measurement of bacterial inhibition. Additionally, Water Guard was assessed for its efficacy as an acidifier, which inhibits intestinal pathogens by interfering with bacterial cell membranes and decreasing the cytoplasmic pH. Acidifiers can also exist in salt forms with similar bactericidal and bacteriostatic properties[39]. This research aims to provide deeper insights into the effectiveness of these agents in controlling bacterial growth and improving food safety. After treatment, the outer membrane of *E. coli O157:H7* is damaged, preventing the aptamer from attaching to it. As a result, the aptasensor cannot capture the antibacterial-treated *E. coli O157:H7* like it can the untreated strain. The evaluation of the antibacterial efficacy of these agents was meticulously performed using DPV techniques, which allowed for precise measurements of the bacterial response to the treatments. Fig. 6A illustrates the decrease in the peak current in the

aptasensor for the dead *E. coli O157:H7* (which was treated with enrofloxacin) was minimal (curve a) compared to untreated *E. coli O157:H7*, which did not receive the antibacterial agent (curve b). Similar results were obtained for Water Guard as an acidifier that kills bacteria (curve c). In addition, the validity of the results obtained from DPV was corroborated through the colony counting method, a widely accepted microbiological technique used to determine the number of viable bacteria following treatment (Fig. 6B). This decisive observation confirms that the aptasensor loses its response entirely upon the loss of cellular viability, unequivocally proving its ability to selectively detect only live, intact cells.

"Please insert Fig. 6 here"

Conclusion and perspective

This study presents a novel electrochemical aptasensor specifically designed for the detection of *E. coli O157:H7*. The sensor utilizes the covalent attachment of aminated aptamers to a reduced graphene oxide and gold nanoparticle nanocomposite, which serves as a highly effective transduction platform. The integration of aminated aptamers enhances both the specificity and sensitivity of the detection process, facilitating the precise identification of *E. coli O157:H7* at low concentrations. This work represents a significant advancement in biosensor technology, particularly in applications related to food safety and environmental monitoring. The covalent coupling established a substantial barrier to electron transfer, resulting in a reduction in peak

currents observed during differential pulse voltammetry measurements. Additionally, this coupling led to an increase in charge transfer resistance, as evidenced by the electrochemical impedance spectroscopy results for the APT/AuNPs/rGO system. Due to its sensitivity, selectivity, rapid response, and reliability, the developed aptasensor enables the detection and quantification of *E. coli O157:H7* across a broad linear dynamic range with a low detection limit in real-world samples. Furthermore, the aptasensor was successfully employed as an ultrasensitive device to evaluate the effect of antibacterial agents on *E. coli O157:H7*. This innovative approach holds considerable potential for future applications in monitoring bacterial pathogens and assessing the efficacy of antibacterial treatments.

Data availability

Data will be available at the academic request from the corresponding author.

Acknowledgments

The authors are highly grateful post-graduate office of Guilan University for the support of this work.

References

1. Albert, V., Ramamurthy, T., Das, S., Dolma, K. G., Majumdar, T. & Baruah, P.J. Comprehending the risk of foodborne and waterborne disease outbreaks: Current situation and control measures with special reference to the Indian scenario. *Heliyon* **10**, e36344 (2024).
2. Rogers, A. R., Mileto, S. J. & Lyras D. Impact of enteric bacterial infections at and beyond the epithelial barrier. *Nat. Rev. Microbiol.* **21**, 260–274 (2023).
3. Lim, J. Y., Yoon, J. W. & Hovde C. J. A brief overview of *Escherichia coli O157:H7* and its plasmid O157. *J. Microbiol. Biotechnol.* **20**, 5–14 (2010).
4. Neill, M. A., Agosti, J. & Rosen, H. Hemorrhagic colitis with *Escherichia coli 0157:H7* preceding adult hemolytic uremic syndrome. *Arch. Intern. Med.* **145**, 2215–2217 (1985).
5. Gopal, A., Yan, L., Kashif, S., Munshi, T., Roy, V. A. & Voelcker, N. H. Biosensors and point-of-care devices for bacterial detection: Rapid diagnostics informing antibiotic therapy. *Adv. Healthc. Mater.* **11**, 2101546 (2022).
6. So, H. M., Park, D. W., Jeon, E. K., Kim, Y. H., Kim, B. S. & Lee, C. K. Detection and titer estimation of *Escherichia coli* using aptamer-functionalized single-walled carbon-nanotube field-effect transistors. *Small* **4**, 197–201 (2008).
7. Galikowska, E., Kunikowska, D., Tokarska-Pietrzak, E., Dziadziuszko, H., Łoś, J. M. & Golec, P. Specific detection of *Salmonella enterica* and

Escherichia coli strains by using ELISA with bacteriophages as recognition agents. *Eur. J. Clin. Microbiol. Infect. Dis.* **30**, 1067–1073 (2011).

8. Johnson, J. R. Development of polymerase chain reaction-based assays for bacterial gene detection. *J. Microbiol. Methods* **41**, 201–209 (2000).
9. Chen, Y., Wang, Z., Liu, Y., Wang, X., Li, Y. & Ma, P. Recent advances in rapid pathogen detection method based on biosensors. *Eur. J. Clin. Microbiol. Infect. Dis.* **37**, 1021–1037 (2018).
10. Thévenot, D. R., Toth, K., Durst, R. A. & Wilson, G. S. Electrochemical biosensors: recommended definitions and classification. *Biosens. Bioelectron.* **16**, 121–131 (2001).
11. Wu, L., Xiong, E., Zhang, X. & Chen, J. Nanomaterials as signal amplification elements in DNA-based electrochemical sensing. *Nano Today* **9**, 197–211 (2014).
12. Pumera, M. Graphene-based nanomaterials and their electrochemistry. *Chem. Soc. Rev.* **39**, 4146–4157 (2010).
13. Ambrosi, A., Bonanni, A., Sofer, Z., Cross, J. S. & Pumera, M. Electrochemistry at chemically modified graphenes, *Chem. Eur. J.* **17**, 10763–10770 (2011).
14. Lawal, A. T. Graphene-based nanocomposites and their applications. A review. *Biosens. Bioelectron.* **141**, 111384 (2019).
15. Andryushina, N., Stroyuk, A., Ustavytska, O., Kurys, Y. I., Kuchmy, S. Y. & Koshechko, V. Graphene oxide composites with silver nanoparticles:

photochemical formation and electrocatalytic activity in the oxidation of methanol and formaldehyde. *Theor. Exp. Chem.* **50**, 155–161 (2014).

16. Darabdhara, G., Das, M. R., Singh, S. P., Rengan, A. K., Szunerits, S. & Boukherroub, R. Ag and Au nanoparticles/reduced graphene oxide composite materials: synthesis and application in diagnostics and therapeutics. *Adv. Colloid Interface Sci.* **271**, 101991 (2019).
17. Szunerits, S., Wang, Q., Vasilescu, A., Li, M. & Boukherroub, R. Graphene/gold nanoparticles for electrochemical sensing, In: Nanocarbons for Electroanalysis. Wiley-VCH, 2017.
18. Xu, C., Wang, X. & Zhu, J. Graphene-metal particle nanocomposites. *J. Phys. Chem. C* **112**, 19841–19845 (2008).
19. Turcheniuk, K., Boukherroub, R. & Szunerits, S. Gold-graphene nanocomposites for sensing and biomedical applications. *J. Mater. Chem. B* **3**, 4301–4324 (2015).
20. Barman, S., Hossain, M. & Park, J. Y. Gold nanoparticles assembled chemically functionalized reduced graphene oxide supported electrochemical immunosensor for ultra-sensitive prostate cancer detection. *J. Electrochem. Soc.* **164**, B234–B239 (2017).
21. Kirsch, J., Siltanen, C., Zhou, Q. & Revzin, A. Biosensor technology: recent advances in threat agent detection and medicine. *Chem. Soc. Rev.* **42**, 8733–8768 (2013).

22. Yüce, M., Kurt, H., Hussain, B. & Budak, H. Systematic evolution of ligands by exponential enrichment for aptamer selection, In: Biomedical Applications of Functionalized Nanomaterials. Elsevier, 2018.

23. Du, Y. & Dong, S. Nucleic acid biosensors: recent advances and perspectives. *Anal. Chem*. **89**, 189–215 (2017).

24. Hianik, T. Aptamer-based biosensors. *Encycl. Interfacial Chem*. **7**, 11–19 (2018).

25. Lim, Y., Y. Lim, Kouzani, A. & Duan, W. Aptasensors: a review. *J. Biomed. Nanotechnol.* **6**, 93–105 (2010).

26. Queirós, R. B., De-Los-Santos-Álvarez, N., Noronha, J. & Sales, M. G. F. A label-free DNA aptamer-based impedance biosensor for the detection of *E. coli O157:H7* outer membrane proteins. *Sens. Actuators B: Chem.* **181**, 766–772 (2013).

27. Brosel-Oliu, S., Ferreira, R., Uria, N., Abramova, N., Gargallo, R. & Muñoz-Pascual, F. X. Novel impedimetric aptasensor for label-free detection of *Escherichia coli O157:H7. Sens. Actuators B: Chem.* **255**, 2988–2995 (2018).

28. Qaanei, M., Taheri, R. A. & Eskandari, K. Electrochemical aptasensor for *Escherichia coli O157:H7* bacteria detection using a nanocomposite of reduced graphene oxide, gold nanoparticles, and polyvinyl alcohol. *Anal. Methods* **13**, 3101–3109 (2021).

29. Wu, W. H., Li, M., Wang, Y., Sun, X., Ouyang, H. X., Wang, L., Li, C. X., Cao, Y. C., Meng, Q. H. & Lu, J. X. Aptasensors for rapid detection of

Escherichia coli O157: H7 and *Salmonella typhimurium*. *Nanoscale Res. Lett.* **7**, 658–665 (2012).

30. Shahrokhian, S. & Ranjbar, S. Aptamer immobilization on amino-functionalized metal-organic frameworks: An ultrasensitive platform for the electrochemical diagnostic of *Escherichia coli O157:H7*. *Analyst* **143**, 3191–3201 (2018).

31. Liu, S., Tian, J., Wang, L. & Sun, X. Microwave-assisted rapid synthesis of Ag nanoparticles/graphene nanosheet composites and their application for hydrogen peroxide detection. *J. Nanoparticle Res.* **13**, 4539–4548 (2011).

32. Fu, Y., Kuang, Y., Huang, Z., Wang, X., Du, N. & Chen, J. Electrochemical co-reduction synthesis of graphene/Au nanocomposites in ionic liquid and their electrochemical activity. *Chem. Phys. Lett.* **499**, 250–253 (2010).

33. El-Hallag, I. S., El-Nahass, M. N., Youssry, S. M. & Kumar, R. Facile in-situ simultaneous electrochemical reduction and deposition of reduced graphene oxide embedded palladium nanoparticles as high-performance electrode materials for supercapacitor with excellent rate capability. *Electrochim. Acta* **314**, 124–134 (2019).

34. Vinodgopal, K., Neppolian, B., Lightcap, I. V., Grieser, F., Ashokkumar, M. & Kamat, P. V. Sonolytic design of graphene-Au nanocomposites. Simultaneous and sequential reduction of graphene oxide and Au(III). *J. Phys. Chem. Lett.* **1**, 1987–1993 (2010).

35. Vázquez-Sánchez, P., Rodríguez-Escudero, M., Burgos, F., Llorente, I., Caballero-Calero, O. & González, M. M. Synthesis of Cu/rGO composites

by chemical and thermal reduction of graphene oxide. *J. Alloys Compd*. **800**, 379–391 (2019).

36. Liu, Y., Gao, L., Sun, J., Wang, Y. & Zhang, J. Stable Nafion-functionalized graphene dispersions for transparent conductingfilms. *Nanotechnology* **20**, 465605 (2009).

37. Lal, A. & Cheeptham, N. Eosin-methylene blue agar plates protocols. American Society for Microbiology, 2016.

38. Trouchon, T. & Lefebvre, S. A review of enrofloxacin for veterinary use. *Open J. Vet. Med.* **6**, 40–58 (2016).

39. Zaldivar, J. & Ingram, L.O. Effect of organic acids on the growth and fermentation of ethanologenic *Escherichia coli LY01. Biotechnol. Bioeng.* **66**, 203–210 (1999).

40. Microbiology of food and animal feeding stuffs – Horizontal method for the detection of *Escherichia coli O157.* BS EN ISO 16654:2001.

41. Wang, Y., Zhao, P., Zhang, H., Chen, W., Su, X. & Suo, B. A simple and rapid real time PCR assay for the detection of *Shigella* and *Escherichia coli* species in raw milk. *J. Verbrauch. Lebensm*. **8**, 313–319 (2013).

42. Galikowska, E. et al. Specific detection of *Salmonella enterica* and *Escherichia coli* strains by using ELISA with bacteriophages as recognition agents. *Eur. J. Clin. Microbiol. Infect. Dis*. **30**, 1067–1073 (2011).

43. Ruan, C. & Li, Y. A bioenzyme electrochemical biosensor coupled with immune-magnetic separation for rapid detection of *Escherichia coli O157:H7* in food samples. *Trans. ASAE* **45**, 249–255 (2002).

44. Zhang, J., Wang, J., Zhang, X. & He, F. Rapid detection of *Escherichia coli* based on 16S rDNA nanogap network electrochemical biosensor. *Biosens. Bioelectron*. **118**, 9–15 (2018).

45. Ye, L., Zhao, G. & Dou, W. An electrochemical immunoassay for *Escherichia coli O157:H7* using double functionalized Au@Pt/SiO_2 nanocomposites and immune-magnetic nanoparticles. *Talanta* **182**, 354–362 (2018).

Authorship contribution statement

Mohadeseh Izadi: Data curation, Investigation, Methodology, Writing – original draft.

Majid Arvand: Conceptualization, Supervision, Visualization, Writing – review & editing.

Funding

There is no external funding source for this research.

Declarations

Competing interests

The authors declare no competing interests.

Ethical statements

This section is not applicable, and no human or animal is studied in this research.

Method	Material	Linear range (CFU/mL)	Measurement time	LOD (CFU/mL)	Ref.
Traditional cultural techniques	Culture media	–	24–48 hour*	30	40
PCR	Primer	10^2 – 10^6	180 min	10^2	41
ELISA	Bacteriophages	–	24–28 hour*	10^6	42
Electrochemical sensor	Antibody	6×10^2 – 6×10^5	120 min	6×10^2	43
Electrochemical biosensor	ssDNA	10^3 – 10^8	180 min	10^2	44
Electrochemical immunoassay	Monoclonal antibody against *E. coli*	3.5×10^3 – 3.5×10^8	165 min*	1.83×10^2	45
Electrochemical aptasensor	Aptamer	6 – 6×10^8	60 min	3.25	This work

*This means that the detection time is not available in the text directly; it is speculated based on the experimental steps in the paper.

Table 1. Comparison between the proposed method and other reported biosensors for detecting *E. coli O157:H7.*

Sample	Added value (CFU/mL)	Detected (CFU/mL)	Recovery (%)	RSD (%)
1	6×10^4	$(5.88 \pm 0.24) \times 10^4$	98.1	4.23
2	6×10^6	$(5.71 \pm 0.15) \times 10^6$	95.3	2.64

Table 2. Detecting *E. coli O157:H7* in certain prepared samples.

Sample	The proposed method (n = 3, x ± SD, CFU/mL)	The plate counting method (n = 3, x ± SD, CFU/mL)	p (n=3)
Farm 1	(3.01 ± 0.34) × 10^2	(3.36 ± 0.32) × 10^2	0.27
Farm 2	(5.81 ± 0.28) × 10^3	(6.10 ± 0.10) × 10^3	0.17

Table 3. Comparison between the proposed method and the plate counting method for the detection of *E. coli O157:H7* at a 95% confidence interval.

Scheme legend

Scheme 1. A diagram illustrating the fabrication process of an aptasensor for detecting *E. coli O157:H7*.

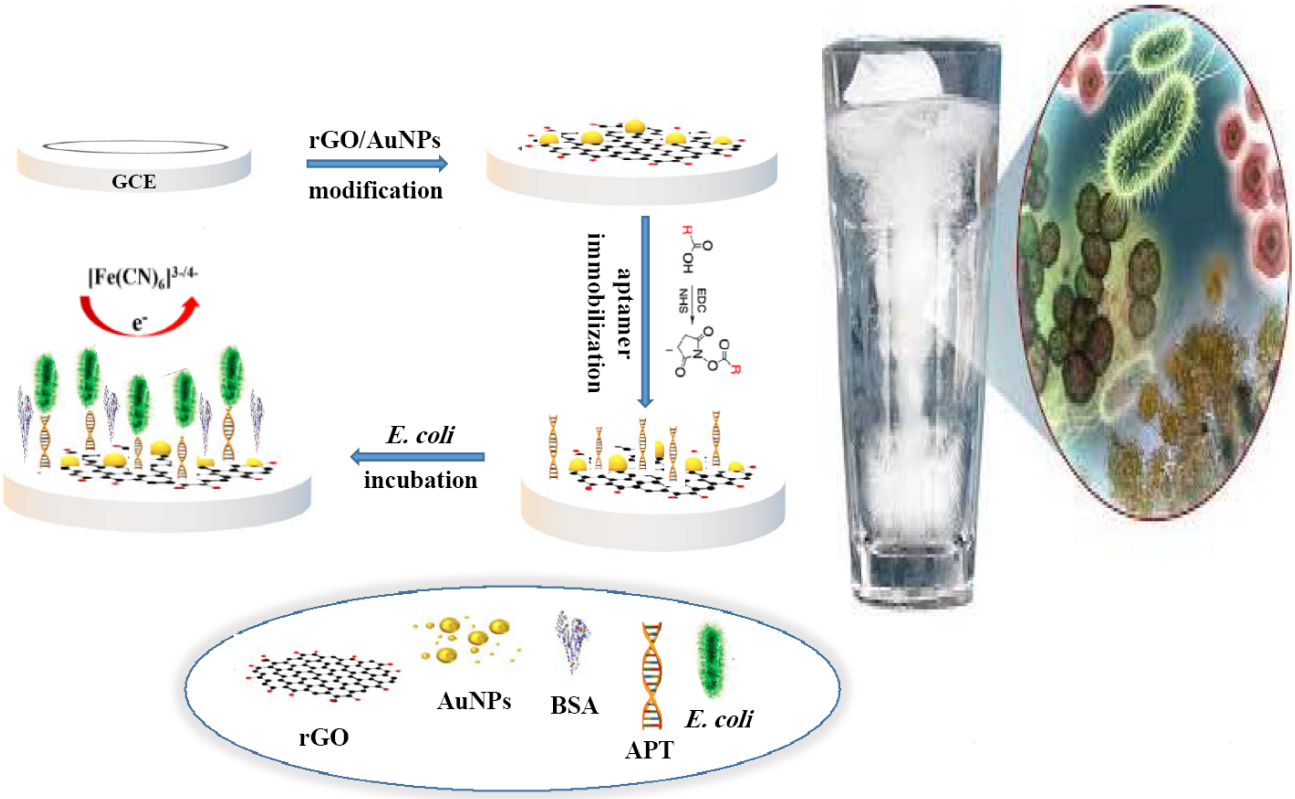

Scheme 1

Figure legends

Fig. 1. (A) FE-SEM surface images of rGO (a–a''), AuNPs/rGO (b–b''), and APT/AuNPs/rGO (c–c'') at different magnifications; (B) EDS analysis of rGO (a), AuNPs/rGO (b), and APT/AuNPs/rGO (c); (C) FT-IR spectra of rGO (a), AuNPs/rGO (b), and APT/AuNPs/rGO (c).

Fig. 2. (A) Cyclic voltammograms (scan rate: 0.1 V/s); (B) Differential pulse voltammograms; (C) Nyquist plots of 0.1 M KCl containing 5 mM $[Fe(CN)_6]^{3-/4-}$ for each step of aptasensor fabrication for *E. coli O157:H7* detection: bare GCE (curve a), rGO/GCE (curve b), AuNPs/rGO/GCE (curve c), APT/AuNPs/rGO/GCE (curve d), and *E. coli*/APT/AuNPs/rGO/GCE (curve e); (D) Differential pulse voltammograms of bare GCE (curve a), rGO/GCE (curve b), AuNPs/GCE (curve c), AuNPs/rGO/GCE (curve d).

Fig. 3. The relationships between the peak current and (A) concentration of rGO, (B) concentration of Au, (C) concentration of APT, (D) incubation time of APT, and (E) incubation time of *E. coli O157:H7*.

Fig. 4. (A) DPV responses of the APT/AuNPs/rGO/GCE sensor incubated with different concentrations of *E. coli O157:H7* (6 to 6×10^8 CFU/mL); (B) Calibration plot of ΔI versus the logarithm of *E. coli O157:H7* concentration.

Fig. 5. Specificity of the electrochemical aptasensor for the target *E. coli O157:H7* (6×10^5 CFU/mL) compared with other bacteria and interfering substances: *Salmonella typhimurium*, *Pseudomonas*

aeruginosa, *Staphylococcus aureus* and *E. coli* K-12) Inset: DPV responses of the aptasensor incubated with *E. coli O157:H7*, *Salmonella typhimurium*, *Pseudomonas aeruginosa*, *Staphylococcus aureus*, *E. coli* K-12 and bacteria-free mode.

Fig. 6. (A) DPV and (B) colony counts results in EMB culture medium of the aptasensor after treatment of *E. coli O157:H7* with enrofloxacin (a), untreated *E. coli O157:H7* (b), and after treatment of *E. coli O157:H7* with Water Guard (c).

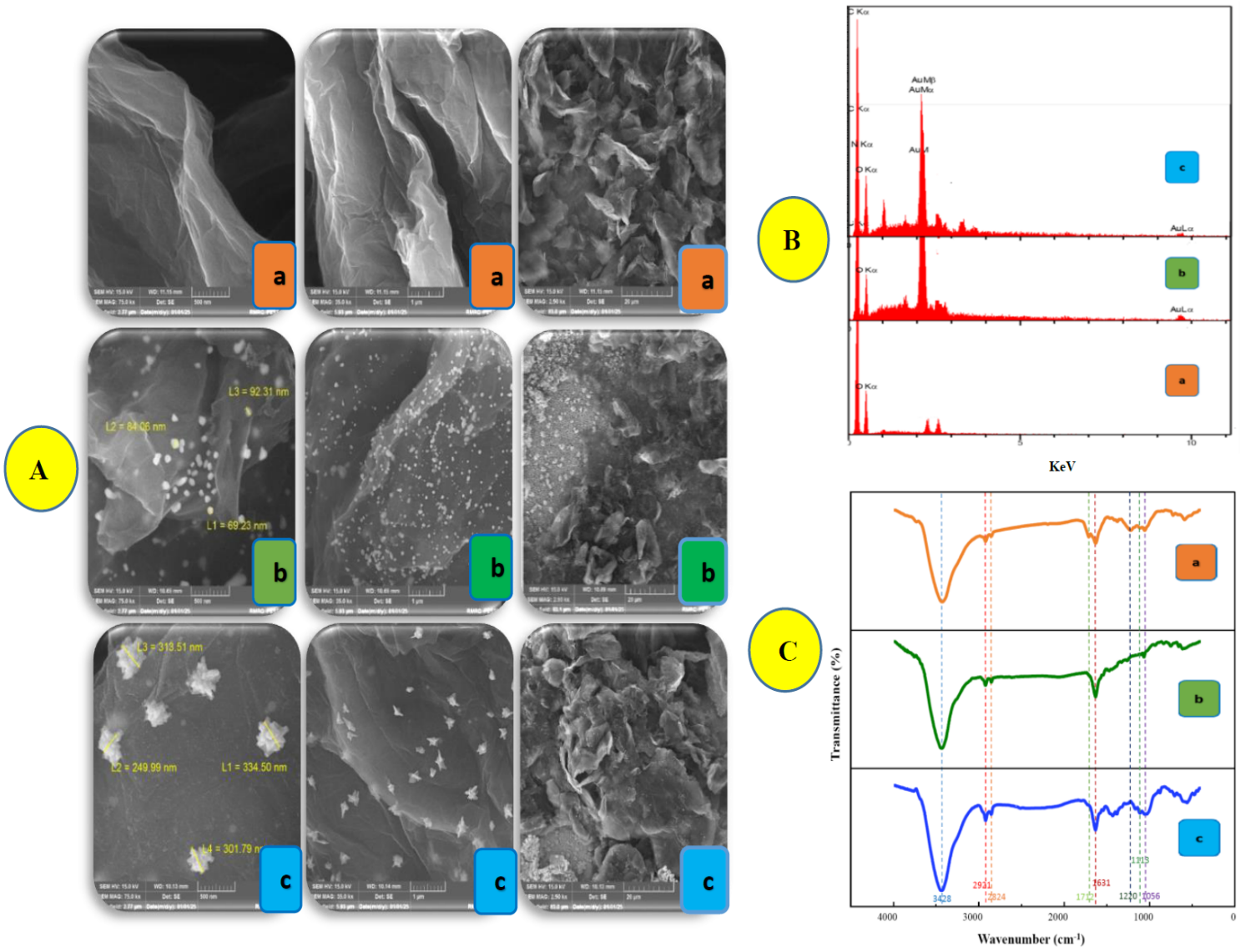
A
a
a
a
L3 = 92.31 nm
L2 = 84.06 nm
L1 = 69.23 nm
b
b
b
L3 = 313.51 nm
L2 = 249.99 nm
L1 = 334.50 nm
c
c
c
B
C Kα
Au Mβ
Au Mα
O Kα
N Kα
Au Lβ
Au Lα
c
b
a
KeV
C
Transmittance (%)
3428
2931
2924
1631
1313
1056
4000
3000
2000
1000
0
Wavenumber (cm⁻¹)

Fig. 1

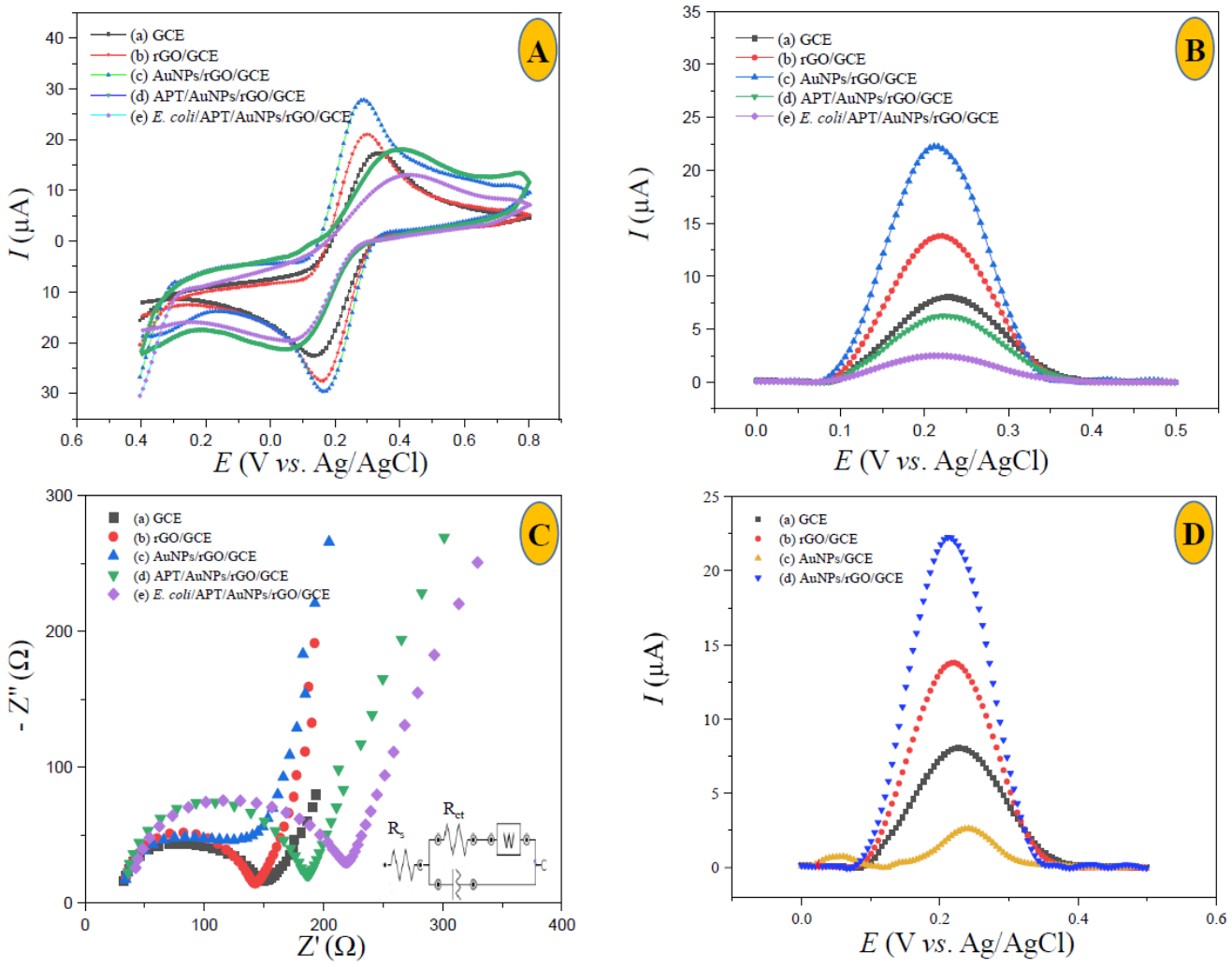
A
(a) GCE
(b) rGO/GCE
(c) AuNPs/rGO/GCE
(d) APT/AuNPs/rGO/GCE
(e) E. coli/APT/AuNPs/rGO/GCE
I (μA)
E (V vs. Ag/AgCl)
B
(a) GCE
(b) rGO/GCE
(c) AuNPs/rGO/GCE
(d) APT/AuNPs/rGO/GCE
(e) E. coli/APT/AuNPs/rGO/GCE
I (μA)
E (V vs. Ag/AgCl)
C
(a) GCE
(b) rGO/GCE
(c) AuNPs/rGO/GCE
(d) APT/AuNPs/rGO/GCE
(e) E. coli/APT/AuNPs/rGO/GCE
- Z'' (Ω)
Z' (Ω)
R_s
R_ct
W
C
D
(a) GCE
(b) rGO/GCE
(c) AuNPs/GCE
(d) AuNPs/rGO/GCE
I (μA)
E (V vs. Ag/AgCl)

Fig. 2

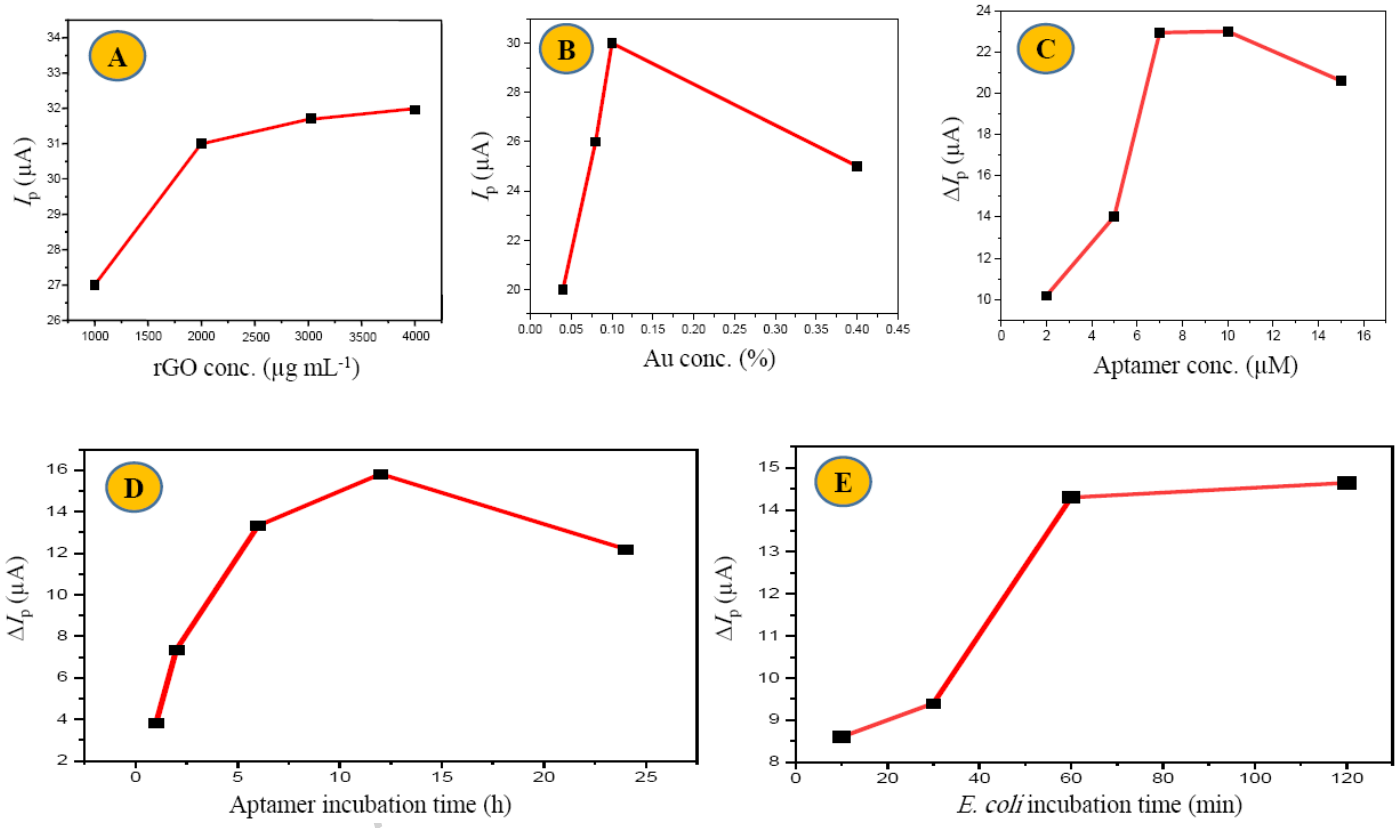
A
I_p (μA)
rGO conc. (μg mL^{-1})
B
I_p (μA)
Au conc. (%)
C
ΔI_p (μA)
Aptamer conc. (μM)
D
ΔI_p (μA)
Aptamer incubation time (h)
E
ΔI_p (μA)
E. coli incubation time (min)

Fig. 3

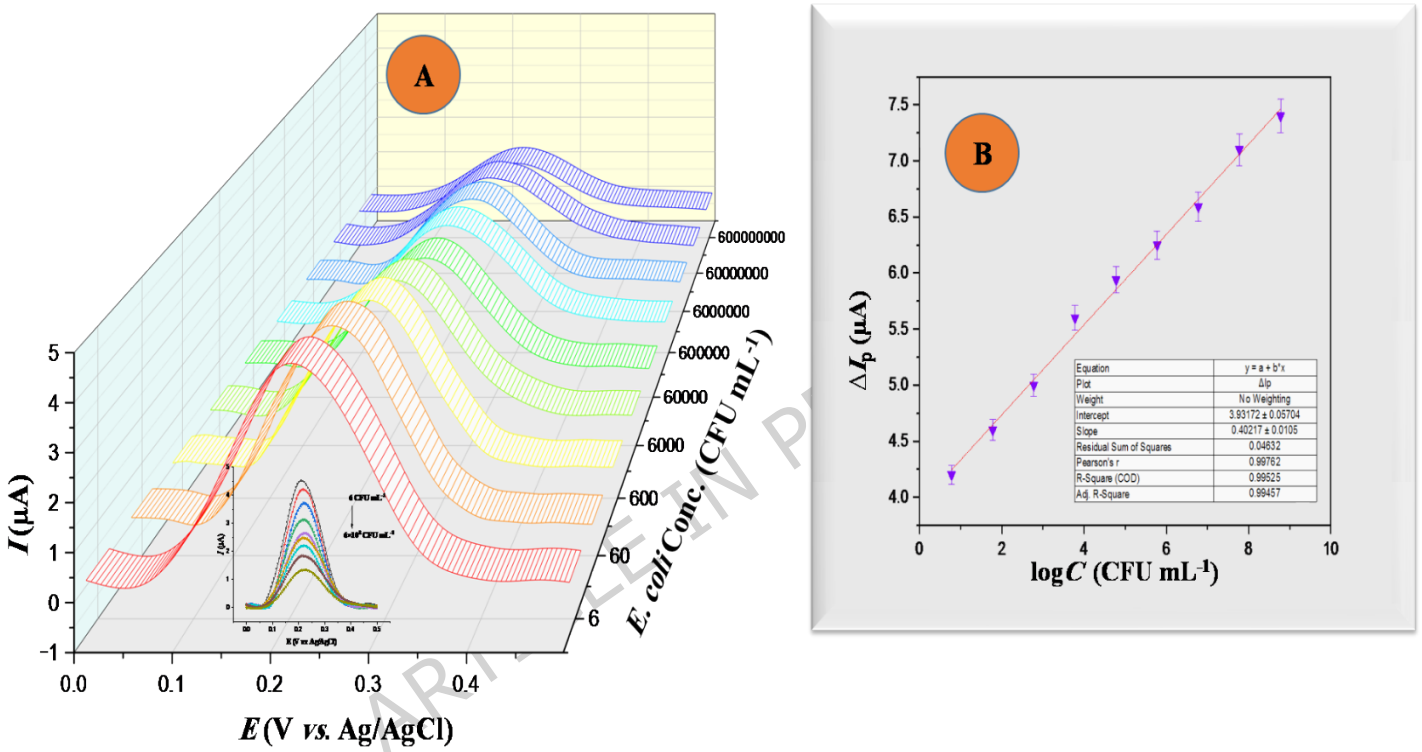
A
B
I (μA)
E (V vs. Ag/AgCl)
E. coli Conc. (CFU mL-1)
600000000
60000000
6000000
600000
60000
6000
600
60
6
ΔIp (μA)
log C (CFU mL-1)
Equation
y = a + b*x
Plot
ΔIp
Weight
No Weighting
Intercept
3.93172 ± 0.05704
Slope
0.40217 ± 0.0105
Residual Sum of Squares
0.04632
Pearson's r
0.99762
R-Square (COD)
0.99525
Adj. R-Square
0.99457

Fig. 4

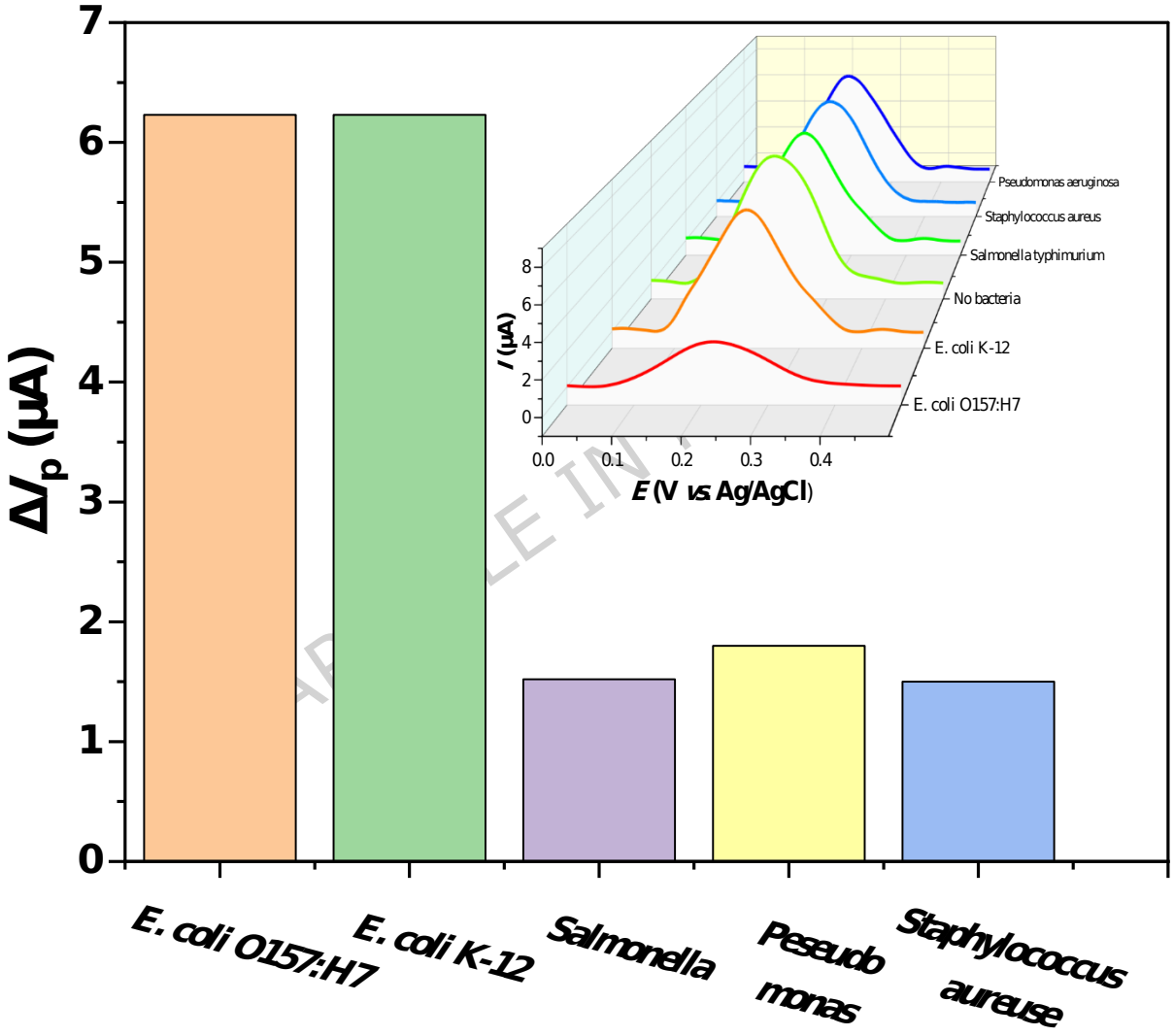
ΔIp (μA)
0
1
2
3
4
5
6
7
E. coli O157:H7
E. coli K-12
Salmonella
Pseudomonas
Staphylococcus aureus
I (μA)
0
2
4
6
8
0.0
0.1
0.2
0.3
0.4
E (V vs Ag/AgCl)
Pseudomonas aeruginosa
Staphylococcus aureus
Salmonella typhimurium
No bacteria
E. coli K-12
E. coli O157:H7

Fig. 5

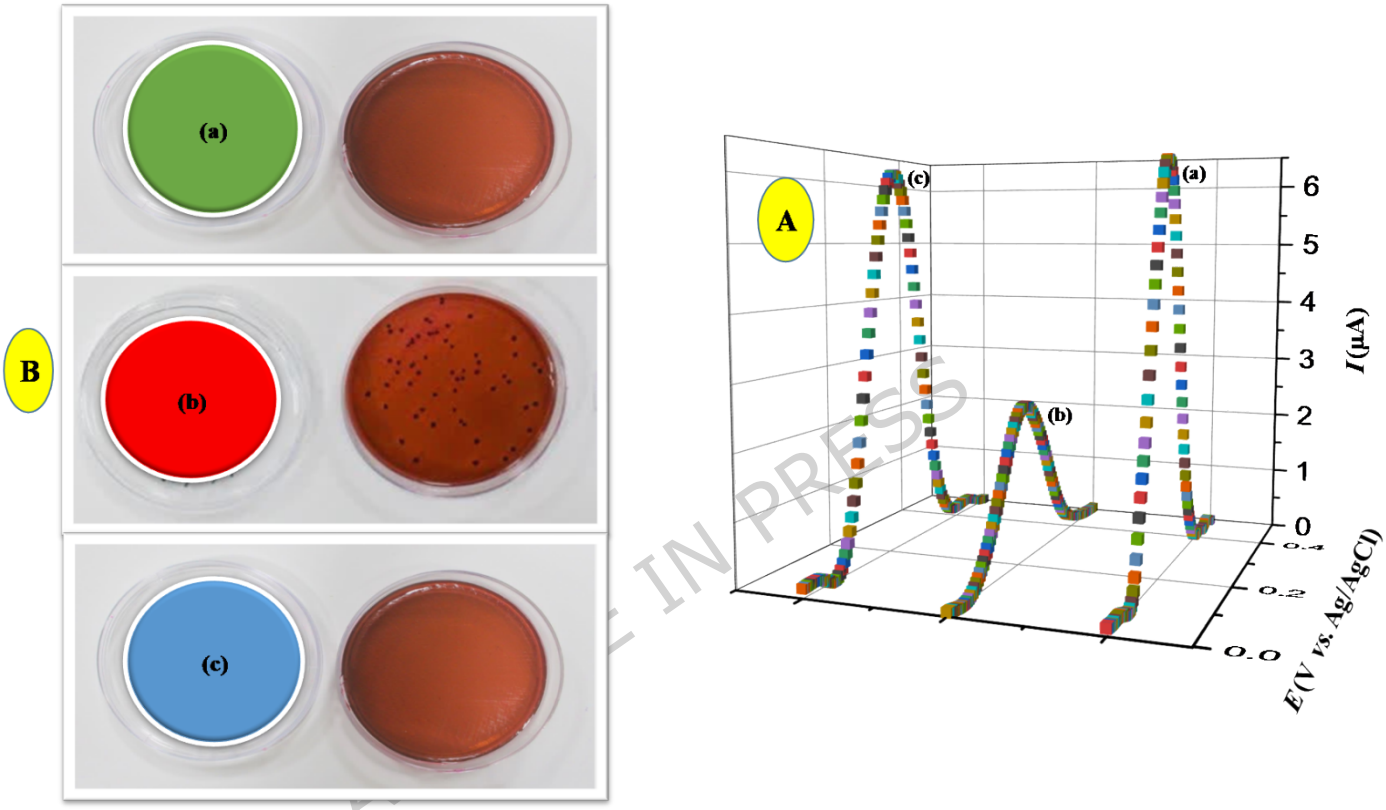

Fig. 6